








Recurring summer and winter droughts from 4.2–3.97 thousand years ago in north India

Alena Giesche ^{1✉}, David A. Hodell ¹, Cameron A. Petrie ², Gerald H. Haug³, Jess F. Adkins⁴, Birgit Plessen⁵, Norbert Marwan ⁶, Harold J. Bradbury ^{1,7}, Adam Hartland ⁸, Amanda D. French⁸ & Sebastian F. M. Breitenbach ⁹

The 4.2-kiloyear event has been described as a global megadrought that transformed multiple Bronze Age complex societies, including the Indus Civilization, located in a sensitive transition zone with a bimodal (summer and winter) rainfall regime. Here we reconstruct changes in summer and winter rainfall from trace elements and oxygen, carbon, and calcium isotopes of a speleothem from Dharamjali Cave in the Himalaya spanning 4.2–3.1 thousand years ago. We find a 230-year period of increased summer and winter drought frequency between 4.2 and 3.97 thousand years ago, with multi-decadal aridity events centered on 4.19, 4.11, and 4.02 thousand years ago. The sub-annually resolved record puts seasonal variability on a human decision-making timescale, and shows that repeated intensely dry periods spanned multiple generations. The record highlights the deficits in winter and summer rainfall during the urban phase of the Indus Civilization, which prompted adaptation through flexible, self-reliant, and drought-resistant agricultural strategies.

¹Godwin Laboratory for Palaeoclimate Research, Department of Earth Sciences, University of Cambridge, Cambridge CB2 3EQ, United Kingdom.

²Department of Archaeology, University of Cambridge, Cambridge CB2 3DZ, United Kingdom. ³Climate Geochemistry Department, Max Planck Institute for Chemistry, Mainz 55020, Germany. ⁴Division of Geological and Planetary Sciences, California Institute of Technology, Pasadena, CA 91125, USA.

⁵Section Climate Dynamics and Landscape Evolution, Helmholtz Centre Potsdam, German Research Centre for Geosciences GFZ, Potsdam 14473, Germany.

⁶Potsdam Institute for Climate Impact Research (PIK), Potsdam 14473, Germany. ⁷Department of Earth, Ocean, and Atmospheric Sciences, University of British Columbia, Vancouver, BC V6T 1Z4, Canada. ⁸Environmental Research Institute, School of Science, Faculty of Science and Engineering, University of Waikato, Hamilton 3216, New Zealand. ⁹Department of Geography and Environmental Sciences, Northumbria University, Newcastle upon Tyne NE1 8ST, UK.

✉email: alena.giesche@gmail.com

Most regions in the world are dominated by either a winter or a summer rain regime. One of the few exceptions is the Indus River Basin and surrounding regions in northwest South Asia that are climatically and environmentally diverse, and feature abrupt transitions between a dominant summer versus winter rain regime (Supplementary Fig. S1 and Supplementary Table S1). Here, we compare the six months of the summer monsoon (May through October, i.e., summer rain) with the remaining winter and spring months (November through April, hereafter referred to as winter rain). For agricultural societies, the seasonal timing and intensity of precipitation are more relevant than total annual rainfall, because a reliable and somewhat predictable timing of water supply is vital for agricultural planning^{1,2}. With a robust multi-seasonal water supply during the mid-Holocene^{3–6}, the Indus River Basin emerged as a favorable area for the development of the complex society known as the Indus Civilization (5000–3600 years ago). However, the intensity of seasonal rainfall in this region appears to have changed considerably since the mid-late Holocene transition c. 4200 years ago. The impact of these changes in seasonal water supply on rainfed agriculture warrants detailed investigation, particularly within the context of archaeological research about societal resilience and decline^{7–12}.

The seasonality component of precipitation variability has increasingly garnered attention in studies from South Asia^{13,14}. Still, the contribution of the Indian Winter Monsoon (IWM) is often overlooked because the Indian Summer Monsoon (ISM) provides >80% of annual rainfall where most studies have been undertaken. Yet, IWM precipitation is particularly important in the Indus River Basin, where precipitation from the winter westerlies dominates the snowpack¹⁵ and late dry season intensity affects agricultural practices and yields. Water availability on the floodplain is also influenced by snow and ice melt during the summertime, which contributes a considerable portion of the annual runoff that feeds the headwaters of the massive Indus/Punjab and Ganges River systems¹⁶. In the western extent of the Indus River Basin, for example, the ratio of winter to summer rainfall exceeds 1:1 (Fig. 1), emphasizing the need to better understand past changes in hydroclimate seasonality of this region.

A consensus is emerging that some form of increased drought affected the landscape of northwest South Asia during the mid-late Holocene transition (i.e., the 4.2 ka event)^{17–20}, although the exact timing and magnitude of the drier period(s) remain uncertain. Paleoclimatic reconstructions suggest a drier than normal mid-late Holocene transition in the winter-rain dominated parts of the Middle East^{21–23}, as well as in parts of the Indian and Asian Summer Monsoon domains of eastern India and China^{1,24–27}. With previous studies exploiting paleoclimate records from either the westerlies-dominated parts of Western Asia or the ISM domain, little is known about climate dynamics in the region of interaction between these two climate regimes. In this study, we focus on the bimodal rainfall regime of northwest South Asia, including the timing and duration of multi-season drought that has been often hindered by large age uncertainties in available paleoclimate records from the region and an over-emphasis on the ISM. Specifically, we aim to reconstruct indications of both the winter and summer rainy seasons from our multi-proxy time series and evaluate the impact these changes may have had on the Indus Civilization.

Although several speleothem records from the Himalaya and northeast India track Holocene ISM strength, and some even cover the mid-late Holocene transition at 4.2 ka BP (kilo annumbefore present, with respect to 1950 CE), e.g., refs. ^{25,27}, very few are located in the western Indian domain²⁸ that simultaneously receives substantial precipitation from the IWM. Furthermore, none of these records incorporate trace element data to independently check conclusions based on speleothem $\delta^{18}\text{O}$. Perhaps due to the difficulty of interpretation, $\delta^{13}\text{C}$ data are also often omitted from discussion although this proxy can inform our understanding of local environmental conditions^{29,30}. Consequently, there is a great need for seasonally-resolved, multi-proxy paleohydroclimatic reconstructions from the Indus River Basin. Here, we aim to characterize hydrological seasonality during the millennium after the mid-late Holocene transition using a speleothem record from the west-central Himalayas. We track the evolution of summer and winter moisture in a seasonally resolved, multi-proxy stalagmite record that begins at 4.2 ka BP from Dharamjali Cave (29.5°N, 80.2°E).

Dharamjali Cave is a shallow (<14 m deep), climatically-responsive cave system with sub-seasonal infiltration dynamics

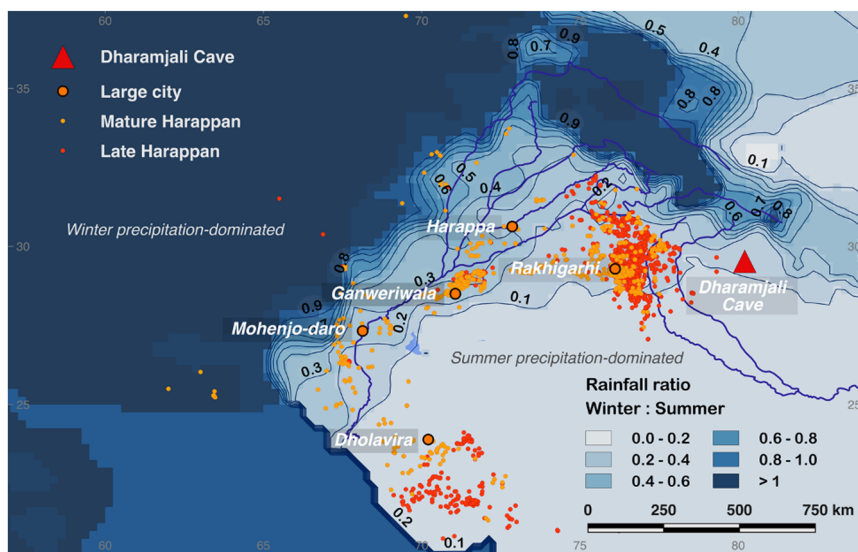


Fig. 1 Local proportion of winter:summer precipitation. Large Indus cities are labeled and shown with the site distribution during the Mature Harappan (c. 4.6–3.9 ka BP, orange) and Late Harappan (c. 3.9–3.6 ka BP, red) periods. Contour lines represent the ratio of IWM (Nov–Apr) to ISM (May–Oct) precipitation based on the 0.25° GPCP v2018 dataset from 1951–2000 rain gauge data⁸⁶.

(see Supplementary Discussion for additional information). The 25-cm-long DHAR-1 stalagmite was located at the far end of the cave. The stalagmite is predominantly aragonite and variations in oxygen isotope values ($\delta^{18}\text{O}_{\text{stal}}$) are used here to reconstruct regional hydrological changes. The $\delta^{18}\text{O}_{\text{stal}}$ record of DHAR-1 reflects seasonal variations in the $\delta^{18}\text{O}$ of rainfall, which is dominated today by the ISM (Supplementary Fig. S2). In northwest South Asia, the moisture source region is the first-order control on ISM $\delta^{18}\text{O}_{\text{precip}}$, which includes the highly evaporated surface waters of the Arabian Sea (0.4 to 0.9‰) and the Bay of Bengal (−2 to 0.5‰)^{31,32}, as well as ^{18}O -enriched rainfall recycled by evapotranspiration from the continent³³ (Supplementary Fig. S3). Strong ISM seasons are generally characterized by low $\delta^{18}\text{O}_{\text{precip}}$ resulting from an increased transport path length (Rayleigh distillation) and reduced sub-cloud evaporation^{34,35}. In contrast to the ISM, the $\delta^{18}\text{O}$ of IWM rainfall is high because it draws more of its moisture from the proximal Arabian Sea^{36,37} and it loses ^{16}O through partial re-evaporation of rainfall in dry air. Winter precipitation is predominantly carried by western disturbances (WDs) that originate over the Mediterranean Sea or mid-Atlantic and travel eastward^{38,39}.

Local environmental conditions can also be traced using speleothem carbon isotopes ($\delta^{13}\text{C}_{\text{stal}}$). Shifts in $\delta^{13}\text{C}_{\text{stal}}$ are driven by a combination of factors, including: overlying vegetation, soil respiration, bedrock dissolution regime, cave ventilation, drip rate, and prior calcite or aragonite precipitation (PCP/PAP) during the driest season or intervals³⁰. The dense C_3 -type forest above Dharamjali Cave today⁴⁰ may well have once featured more drought-resistant C_4 -type vegetation, as reconstructed for parts of the northwestern Himalaya c. 4 ka BP^{41,42}. In particular, the growth and resilience of the Chir pine species (*Pinus roxburghii*) dominantly present above Dharamjali cave today⁴⁰ is known to be particularly sensitive to winter and spring rainfall^{43,44}. Thus, we might expect increasing $\delta^{13}\text{C}_{\text{stal}}$ values in response to long-term drought-induced vegetation changes, particularly driven by winter and spring moisture limitation, e.g., refs. 43–46. Other factors influencing $\delta^{13}\text{C}_{\text{stal}}$ are relevant at the seasonal to interannual scale, and fluctuate more dynamically during the winter season. For example, in winter the cave air temperature exceeds that of the outside air (promoting enhanced ventilation), drip rate slows to 3–8 drops/min compared to 20–30 drops/min in summer⁴⁰, and PAP is most likely to occur in air-filled voids in the epikarst as potential evapotranspiration exceeds precipitation during the drier winter months. Taken together, increased cave ventilation, lower drip rates, and PAP in wintertime all lead to higher $\delta^{13}\text{C}_{\text{stal}}$ and more bedrock-like values, though the colder winter season also features minimal soil respiration that acts to lower $\delta^{13}\text{C}_{\text{stal}}$. Cave CO_2 monitoring data are not available at Dharamjali Cave, but the sum of mechanisms suggests that cooler, longer, and/or drier winters lead to higher $\delta^{13}\text{C}_{\text{stal}}$ values (see Supplementary Discussion for a more extensive analysis of $\delta^{13}\text{C}$). Seasonal cave monitoring would be required to disentangle the primary effects responsible for $\delta^{13}\text{C}_{\text{stal}}$ values and provide more certainty about their paleoclimatic interpretation.

Shifts in speleothem calcium isotopes, specifically $\delta^{44/40}\text{Ca}$, are similarly useful aridity proxies via PCP/PAP processes in caves, and have been used to interpret past rainfall amount more quantitatively than is possible with $\delta^{18}\text{O}$ ^{47–49}. During carbonate precipitation, ^{40}Ca is preferentially incorporated into the solid phase relative to the heavier isotope ^{44}Ca . Thus, water that infiltrates more slowly and is given more time to degas and precipitate before reaching the stalagmite under drier conditions will yield a smaller difference between the two isotopes and a resulting higher $\delta^{44/40}\text{Ca}_{\text{stal}}$. This concept underlies the

interpretation of any PCP or PAP proxy, and directly connects this proxy to rainfall amount⁵⁰. Importantly, an aridity threshold is required before any PCP/PAP effects are noticeable—therefore, such proxies tend to mainly reflect changes in the length or severity of the driest season because only an extreme change in wet season rainfall amount would reduce cave saturation to an appreciable degree to cross the threshold for this proxy^{14,48}.

Additionally, we use trace element changes of DHAR-1 as independent tracers of past hydrologic changes^{50–52}. The distribution of U^{2+} , Sr^{2+} , and Ba^{2+} in aragonite speleothems reacts to PAP dynamics in the epikarst^{53,54}. With intensified and/or prolonged dry-season (winter) aridity and associated PAP, concentrations of uranium ($D_{\text{U}(\text{Ar})} \gg 1$) and strontium ($D_{\text{Sr}(\text{Ar})} > 1$) are expected to decrease in the resulting speleothem, while barium ($D_{\text{Ba}(\text{Ar})} \sim 1$) appears to be a less reliable indicator, although it may also decrease⁵⁴. Research in calcite stalagmites further suggests that transition metals such as Zn^{2+} , Ni^{2+} , Cu^{2+} , and Co^{2+} increase with lower drip rates due to the dominance of ligand-bonded metal dissociation over prior calcite precipitation (PCP)^{55,56}. We investigate preliminary transition metal relationships in the DHAR-1 data to understand whether such drip rate effects may also relate to ISM rainfall intensity or wintertime PAP in this aragonite speleothem.

Results and discussion

Stalagmite age model and mineralogy. The age model for the multi-proxy record from stalagmite DHAR-1 is based on twelve U-series dates (Supplementary Table S2) that span 4.2–2.55 ka BP with an average 2σ error of ± 18 years. Depth-age modeling was completed for each proxy using the COPRA routine⁵⁷. Low growth rates of $90 \mu\text{m}/\text{year}$ in the older section (4.2–3.1 ka BP) were followed by higher deposition rates of $200 \mu\text{m}/\text{year}$ for 3.1–2.55 ka BP (Supplementary Fig. S4). The higher growth rate after 3.1 ka BP mainly reflects an increase in porosity associated with changes in trace element concentration and crystal growth fabric. The simultaneous shift in growth axis at 3.1 ka BP suggests a change in drip flow path, related to a climatic or tectonic trigger (Supplementary Discussion), and we therefore focus our climatic interpretation on the earlier undisturbed interval between 4.2 and 3.1 ka BP (all data are available in the online repository).

At the base of DHAR-1, X-ray diffraction analysis confirms a mineralogical transition from a 3-mm basal calcite layer to primary aragonite for the rest of the sample over 4.2–2.55 ka BP. Trace element data corroborates this shift with distinct changes of several element/calcium ratios, where Mg/Ca is higher in calcite compared to aragonite and Sr/Ca, U/Ca, and Ba/Ca are all lower in calcite than aragonite (Fig. 2a). This calcite-to-aragonite transition in itself supports a shift towards drier conditions because aragonite is preferentially deposited with more extensive evaporation and PCP or PAP^{58–60}. The darker, dirty layer between the calcite-aragonite transition marks a hiatus between the two deposition phases (Supplementary Fig. S5).

Oxygen, carbon, and calcium stable isotopes. A profile of 750 oxygen and carbon stable isotope samples was resolved at 100–300 μm (annually) over the entire sample 4.2 to 2.55 ka BP (GFZ Potsdam), and extended with 876 samples milled at 50 μm (sub-annual) resolution between 4.2 and 3.6 ka BP at the University of Cambridge (Fig. 2). Laser ablation element data was obtained at c. 25 μm resolution at the University of Waikato (Supplementary Fig. S6). Both the low and high resolution DHAR-1 isotope series show excellent agreement in the region of overlap. Furthermore, DHAR-1 replicates the lower resolved and less-well dated DH-1 record from the same cave⁶¹ (Supplementary Fig. S7).

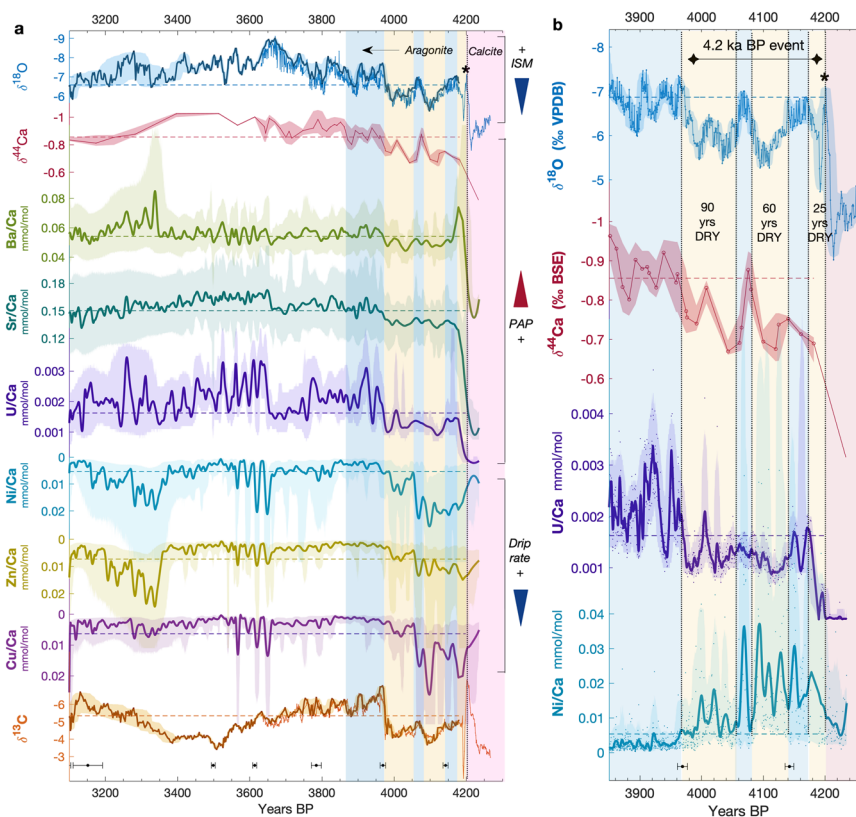


Fig. 2 DHAR-1 proxies from 4.2 to 3.1 ka BP. **a** 4.27–3.1 ka BP DHAR-1 record with high-resolution $\delta^{18}\text{O}$, $\delta^{44}\text{Ca}$, and $\delta^{13}\text{C}$ stable isotope time series (note reverse axes) and Ba/Ca, Sr/Ca, U/Ca, Ni/Ca, Zn/Ca, and Cu/Ca trace element data shown as 20-year LOESS smoothing curves. Dominant processes for the proxies are indicated with arrows on the right (Indian Summer Monsoon, prior aragonite precipitation, and drip rate). $\delta^{13}\text{C}$ is not specified because it is affected by a (variable) combination of prior aragonite precipitation, cave ventilation, and long-term soil carbon changes driven by vegetation above the cave. **b** 4.27–3.85 ka BP in more detail covering the 4.2 ka event, with $\delta^{18}\text{O}$ and $\delta^{44}\text{Ca}$ stable isotope time series, and U/Ca and Ni/Ca with 10-year LOESS smoothing curves. The asterisk represents the transition from calcite to aragonite after a hiatus. For each series, shaded envelopes represent the 2.5 and 97.5% proxy confidence intervals, and horizontal dashed lines show the mean value over 4.2–3.1 ka BP. Vertical shaded bars denote relatively dry (yellow) and wet (blue) intervals between 4.27 and 3.85 ka BP. U-series dates with $\pm 2\sigma$ error bars are shown at the bottom of the graphs above the lower age axes.

The majority of the $\delta^{44}\text{Ca}_{\text{stal}}$ measurements (49 out of 61 samples) focused on the period of greatest interest from 4.2 to 3.6 ka BP, yielding a nearly decadal resolution (1 sample per 12.6 years). Values during this period ranged from -1.06 to -0.27‰ (mean = -0.84‰). The prominent positive excursion in the $\delta^{44}\text{Ca}_{\text{stal}}$ results closely mirror both $\delta^{18}\text{O}_{\text{stal}}$ and $\delta^{13}\text{C}_{\text{stal}}$ between 4.2 and 3.97 ka BP (Fig. 2b), a strong indication for a lengthy, multi-season period of lower rainfall. The data from the following period between 3.97 and c. 3.4 ka BP shows more negative values in all proxies, though with divergent trends: $\delta^{18}\text{O}_{\text{stal}}$ trends negative, $\delta^{44}\text{Ca}_{\text{stal}}$ has no discernible trend, and $\delta^{13}\text{C}_{\text{stal}}$ trends positive. This pattern suggests a less dominant PAP forcing for $\delta^{44}\text{Ca}$ and $\delta^{13}\text{C}$ after crossing a moisture threshold (e.g., an extended ISM season could ameliorate PAP processes)^{14,48}. The positive trend in $\delta^{13}\text{C}_{\text{stal}}$ may relate to strengthening winter cave ventilation driven by cooling temperatures outside the cave and related CO_2 dynamics, decreasing cave drip rates and thus enhanced CO_2 degassing in winter (summer cannot be a candidate because $\delta^{18}\text{O}_{\text{stal}}$ shows the ISM rainfall increased), and/or a long-term shift to more winter-drought-resistant C_4 -type vegetation above the cave, e.g., refs. ^{43–46} (see Supplementary Discussion for additional $\delta^{13}\text{C}$ analysis).

Trace elements tracking prior aragonite precipitation, drip rate, and redox conditions. The trace element profiles (seasonal resolution at 25 μm) add further evidence to our interpretation of the DHAR-1 proxies. A notable grouping of U^{2+} , Sr^{2+} , and Ba^{2+}

in PC2 of a Principal Component Analysis (PCA) on the trace element profile over 4.2–3.1 ka BP (Fig. 3), and their positive correlation (Supplementary Fig. S8), suggest that PAP influences the concentration of these elements. In particular, U^{2+} and Sr^{2+} consistently follow the other PAP proxy, $\delta^{44}\text{Ca}$ (Fig. 2a). The cluster of transition metals Zn^{2+} , Ni^{2+} , and Cu^{2+} in PC3 (Fig. 3) highlights elements that may respond to drip-rate changes in aragonite stalagmites⁵⁵ (see Supplementary Discussion for additional transition metal discussion). Indeed, the transition metals all indicate lower drip rates during the period of less rainfall from 4.2–3.97 ka BP. By extension, low drip rates also occur around 3.6 ka BP and again after 3.3 ka BP.

Furthermore, the redox-sensitive ions of S^{2+} , Mn^{2+} , Fe^{2+} , and Cr^{2+} , together with Mg^{2+} and Si^{2+} , can be separated from the other two groups in PC3 (Fig. 3). While higher Mg and Si likely reflect increased input of detrital material or enhanced weathering of fresh bedrock material, the grouping of redox-sensitive elements suggests that the soil above the epikarst may be sensitive to saturated conditions that enable a series of redox processes⁶². Notably, the S/Ca record deviates after 3.72 ka BP (marking a period of higher and more variable sulfur content), and occasionally aligns with the PAP (U/Ca, Sr/Ca) and drip rate (Zn/Ca, Ni/Ca) proxies (Supplementary Figs. S6 and S9). This dynamic suggests that another environmental factor emerges after 3.72 ka BP—possibly related to redox conditions (e.g., waterlogging) in the overlying soils. Concurrent peaks in the redox-sensitive elements (Supplementary Fig. S6) are thus interpreted as periods when a more saturated drip flow path promoted water

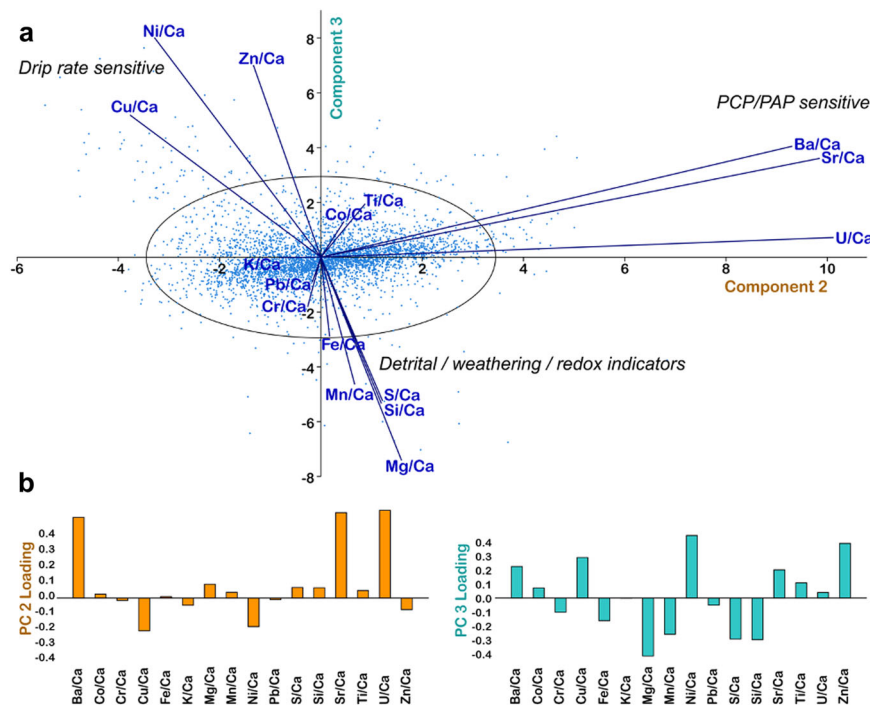


Fig. 3 Principal component analysis from 4.2–3.1 ka BP. **a** Principal components 2 and 3 of the LA-ICP-MS dataset for the aragonite-only bottom half of DHAR-1B (4.2–3.1 ka BP) with a 95% confidence ellipse (black circle), showing distinct groups of the drip-rate-sensitive transition metals Ni, Zn, and Cu, the PAP-sensitive trace elements Ba, Sr, and U, and the redox-related trace elements of Fe, S, Cr, and Mn. **b** Loadings for PC2 (12.4% of variance) and PC3 (9% of variance). Statistics were calculated and the figure was generated using PAST 4.10 software⁸⁷. Note that PC1 (28.8% of variance) is not shown—the loadings indicate a dominance of U/Ca over other elemental ratios.

retention—suggestive of a hydrological (and perhaps ecological) shift associated with increased soil moisture and change in the seasonal timing of precipitation.

Multi-proxy interpretation. Correlations between individual proxies ($\delta^{44}\text{Ca}$, $\delta^{13}\text{C}$, $\delta^{18}\text{O}$, Sr/Ca, S/Ca, Ba/Ca, Zn/Ca, and Ni/Ca) were examined for three discrete time periods over 4.14–3.61 ka BP (Supplementary Fig. S9). This analysis highlights incongruous relationships between several pairs of proxies after 3.94 ka BP or 3.72 ka BP (e.g., $\delta^{13}\text{C}$ with $\delta^{18}\text{O}$, Sr/Ca, and U/Ca; $\delta^{18}\text{O}$ with Zn/Ca and Ni/Ca; Sr/Ca with Zn/Ca and Ni/Ca), suggesting that certain proxies display threshold behavior (e.g., PAP occurs only during extreme drought). A nuanced interpretation may be appropriate in some periods; for example, c. 3.6 and 3.3 ka BP when trace elements indicate a decreased drip rate but also less PAP, which could result from a lengthened ISM season that distributes the same amount of moisture over a longer wet season. After 3.4 ka BP, the $\delta^{13}\text{C}$ and drip rate proxies (Cu/Ca, Zn/Ca, and Ni/Ca) consistently indicate wetter and/or warming conditions (with $\delta^{13}\text{C}$ suggesting either vegetation that thrives in wetter conditions, less CO_2 degassing due to wet conditions, or less ventilation from warming), and this appears related to winter precipitation because the ISM proxies show a decrease in summer precipitation. Drip rate could reflect both ISM and IWM precipitation, and thereby requires reliable ISM or IWM proxies to distinguish a seasonal interpretation. In contrast, the correlation between $\delta^{13}\text{C}$ and the drip rate proxies breaks down from 3.7 to 3.4 ka BP. Given that $\delta^{13}\text{C}$ is influenced by a number of factors³⁰, it is plausible that ventilation or CO_2 degassing could be the primary influence on $\delta^{13}\text{C}$ during some periods, while gradual shifts in soil carbon above the cave could influence the overall (centennial-scale) trends. For example, if winter precipitation decreased over decades to centuries, it is possible that winter- and spring-drought sensitive trees^{43–46}

would be increasingly replaced by C_4 -type plants, leading to higher $\delta^{13}\text{C}$ (as seen between 3.9 and 3.4 ka BP).

Of the entire DHAR-1 record, the 230-year period after 4.2 ka BP stands out for its above-average $\delta^{18}\text{O}$, $\delta^{44}\text{Ca}$, $\delta^{13}\text{C}$, Ni/Ca, Zn/Ca, and Cu/Ca, while Ba/Ca, Sr/Ca, and U/Ca values are all below-average (Fig. 2a). This agreement across all proxies reveals three distinct dry periods lasting 25–90 years each, which correspond to the general timing of the ‘4.2 ka event’ that is associated with the mid-late Holocene transition (Fig. 2b). After 3.97 ka BP, some divergent trends emerge in ISM ($\delta^{18}\text{O}$), PAP ($\delta^{44}\text{Ca}$, $\delta^{13}\text{C}$, U/Ca, Sr/Ca) and drip rate (Zn/Ca and Ni/Ca) proxies, suggesting that the drought threshold was not consistently passed in both seasons and other environmental factors assumed a more prominent role. While ISM rainfall increases after 3.97 ka BP, PAP proxies indicate a more muted recovery (or simply stabilization) of annual precipitation, with drip rate recovering until a decrease around 3.6 ka BP, and $\delta^{13}\text{C}$ trends point to cooling (enhanced ventilation) and/or drying conditions in wintertime (either via more degassing from lower drip rate, or a shift in soil carbon). Such a shift in seasonality towards more pronounced rainfall contrast between summer and winter may have contributed to long term changes in vegetation composition (particularly away from winter-drought-sensitive C_3 -type trees to more drought-tolerant C_4 -type grasses) that ultimately altered the water retention and drainage properties of the soil above the cave (redox conditions indicated by S/Ca, Fe/Ca, Mn/Ca, Cr/Ca). We note that the $\delta^{13}\text{C}$ proxy is susceptible to multiple influences, while the Ni/Ca, Zn/Ca, and Cu/Ca seem to be reliable proxies for drip rate, even though they are novel and untested in aragonite speleothems. Keeping this caveat in mind, we cautiously interpret the multi-proxy record as an increase in seasonality with stronger ISM seasons and longer or drier winters between 3.97 and 3.4 ka BP, followed by decreased seasonality as the ISM weakens and winter moisture picks up again from 3.4 to 3.1 ka BP.

Since Dharamjali Cave sits in a transition zone influenced by winter westerlies and the ISM, it is likely that multidecadal shifts in Northern Hemisphere insolation, the Atlantic Meridional Oscillation (AMO) and North Atlantic Oscillation (NAO), as well as the Pacific Decadal Oscillation (PDO) and El Niño–Southern Oscillation (ENSO) would play a role in modulating the strength of the dry and wet season rainfall systems and total annual rainfall over Dharamjali Cave, as it does in northeast India⁶³. Along with negative NAO conditions, atmospheric blocking patterns over Europe can translate to drier westerlies in the Mediterranean and western Asia, which is one mechanism proposed for the 4.2 ka event^{1,64,65}. Furthermore, warm PDO or ENSO phases have been linked to a weaker ISM with less rainfall in northeast India^{14,66,67}.

4.2 ka event. DHAR-1 provides vital insight into the seasonality of the 4.2 ka event and the millennium thereafter. The unambiguous agreement between all moisture proxies (ISM, PAP, drip rate) from 4.2 to 3.97 ka BP provides a convincing set of evidence for a multi-season drought that overprinted all other environmental forcings in the DHAR-1 cave system. Although we lack early-Holocene stalagmite records older than 4.2 ka BP from Dharamjali Cave, we are still able to put the DHAR-1 reconstruction into perspective with post-4.2 ka BP climate conditions. Our multi-proxy time series allows us to characterize seasonality changes during the 4.2 ka event (dry in both seasons), the duration of the dry periods (25–90 years), the timing of ISM recovery (after 3.97 ka BP), and environmental and seasonality changes after 3.97 ka BP.

We compare DHAR-1 with nearby records to provide a more (pan)regional view of mid-Holocene climate change (see locations of studies from Fig. 4 in Supplementary Fig. S1). A highly resolved and well dated stalagmite ML.1 from Mawmluh Cave shows a decrease in rainfall closer to 4.0 ka BP that does not recover over the next centuries²⁷ (Fig. 4a), whereas another stalagmite record (KM-A) from Mawmluh suggests lower rainfall at 4.1 ka BP and subsequent recovery by 3.9 ka BP²⁵. The discrepancy between both Mawmluh records may be due to dating and dissolution issues in the KM-A record²⁷, thus we refer to the more recent and well-dated ML.1 reconstruction from this cave. The discrepancy in timing of drought between the similarly well-dated and highly-resolved ML.1 and DHAR-1 records is most likely due to regional variation in ISM behavior. The distance between Mawmluh and Dharamjali caves is approximately 1200 km (east-west), where Mawmluh cave sits much closer to the Bay of Bengal moisture source for the ISM and is completely removed from the westerlies/IWM influence in winter. Therefore, it would be reasonable to expect a reduction in ISM rainfall to affect more distant locations like Dharamjali more severely. We also cannot exclude the possibility that changes to the Arabian Sea branch of the ISM might have decreased ISM moisture in the western regions of India (and thereby primarily impact the Dharamjali record), while the Bay of Bengal branch may have been impacted differently^{32,68}.

Similar to Dharamjali, the ISM record of marine core 63KA from the northeast Arabian Sea shows a double-peaked increase in $\delta^{18}\text{O}$ values centered around 4.1 and 4.0 ka BP that coincides with reduced Indus River outflow, which is followed by a recovery after 3.9 ka BP^{18,69} (Fig. 4b). In the Red Sea, high-salinity conditions are observed over the same period⁷⁰ (Fig. 4c). The 4.2 ka event is typically characterized as an undifferentiated multi-century-scale drought, but the DHAR-1 record provides considerably finer-grained detail over the 4.2 ka event and reveals three major phases of lower rainfall peaking at 4.19, 4.11, and 4.02 ka BP, each lasting 25–90 years and separated by 20–30-year-long recovery phases (Figs. 2b and 4d, e).

Notably, relatively wet winter conditions are apparent for several centuries preceding the 4.2 ka event, as demonstrated by the Gol-e-Zard speleothem record from Iran²³ (Fig. 4f) as well as enhanced upper ocean mixing and more evaporative, windy winter conditions in the NE Arabian Sea inferred from the 63KA marine record⁶⁹ (Fig. 4g). During the mid-late Holocene transition, upper ocean mixing was subdued⁶⁹ and regionally arid and dusty conditions affected Western Asia for 290 years after 4.26 ka BP²³.

In contrast, the Sahiya Cave speleothem record (SAH-2), located c. 250 km further west than Dharamjali Cave, shows relatively low $\delta^{18}\text{O}$ values between 4.2 and 3.5 ka BP that would indicate a stronger ISM or IWM²⁸. However, a prominent growth rate minimum (2–3 $\mu\text{m}/\text{year}$) in the SAH-2 record during this interval suggests that a reduced water supply to the stalagmite may have affected its growth and signal a depositional hiatus, which could mask a drought and explain the discrepancy with the DHAR-1 record (Fig. 4h). Consequently, additional records with multiple proxies from this cave or nearby sites would be useful additions to clarify its interpretation.

Overall, the dry winter and summer conditions between c. 4.2 ka BP and 3.9 ka BP resulted in aeolian dust spikes in the Arabian Sea⁷¹ (Fig. 4i) and drying of lakes in continental India, e.g., refs. 19,20 (Fig. 4j). While ISM strength was already slowly deteriorating prior to the 4.2 ka event due to decreasing Northern Hemisphere summer insolation, e.g., refs. 4,69, the shift from exceptionally wet to markedly dry winter conditions would be most perceptible in regions such as the Indus River Basin that receive a high proportion of winter rain.

Cultural implications. Importantly, DHAR-1's precise age model allows us to sub-divide the 4.2 ka event into separate severe arid phases within a 230-year drier-than-normal period. Records of the 4.2 ka event often portray it as a single mega-drought that lasted around 100–200 years. The high resolution of the DHAR-1 record advances our understanding by revealing at least three major dry periods within this period lasting 25–90 years each. Since the 4.2 ka event is significant in part because of its impact on large, complex Bronze Age civilizations, DHAR-1's level of temporal resolution is applicable to the human decision-making timescale. While farmers and traders may be able to temporarily adjust practices in the face of a multi-year drought, a severe multi-decadal dry period affecting several generations of people would prompt more far-reaching and permanent adaptations or even population movement—particularly after the peak of the final and longest 90-year drought by 4.02 ka BP.

Paleoclimate data suggest that the Early Harappan phase (c. 5.0–4.6 ka BP) and the first half of the Mature Harappan phase (c. 4.6–3.9 ka BP) of the Indus Civilization were accompanied by relatively strong winter westerlies and associated IWM precipitation^{23,69}, but concurrently declining ISM precipitation^{69,72–74}. After 4.2 ka BP, Harappa (an urban center within the winter-rain dominated region) began to show signs of decline such as disease outbreaks and deteriorating urban systems^{8,9}. Based on the DHAR-1 record, the three major phases of lower rainfall after 4.2 ka BP each lasted >25 years over a c. 230-year period, and would have had long-term environmental impacts on daily and year-round access to water, predictability of rainfall, and the extent, timing, and recurrence of river flooding. Moreover, the adverse effects of droughts on rainfed and floodplain agriculture would have been amplified if both rainfall seasons weakened or failed entirely. These periods of lower rainfall are particularly long in human timescales, and would have impacted multiple generations of individual populations and influenced their subsistence practices. The diversity of crops and

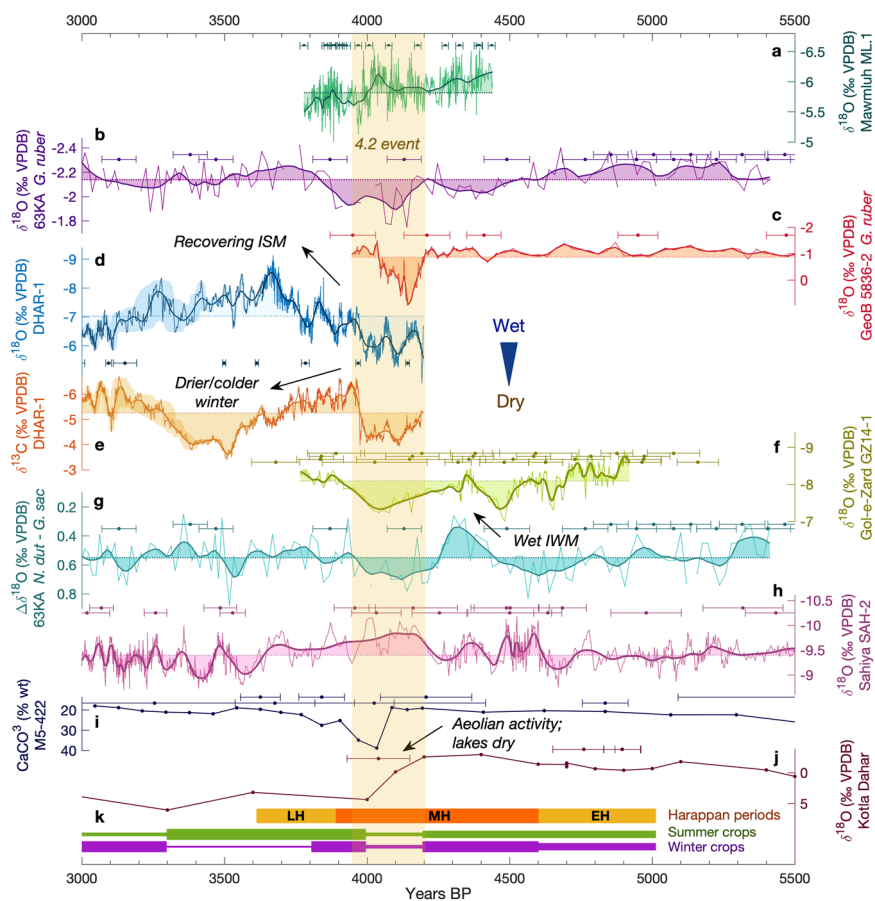


Fig. 4 Comparison of northwest South Asian records over the 4.2 ka event. **a** Indian Mawmluh stalagmite ML.1 $\delta^{18}\text{O}$ ²⁷, **b** Arabian Sea marine core 63KA $\delta^{18}\text{O}$ of *G. ruber* 400–500 μm ⁶⁹, **c** Red Sea marine core GeoB 5836-2 $\delta^{18}\text{O}$ of *G. ruber*⁷⁰, **d** Indian stalagmite DHAR-1 $\delta^{18}\text{O}$ (this study), **e** DHAR-1 $\delta^{13}\text{C}$ (this study), **f** Iranian Gol-e-Zard stalagmite GZ14-1 $\delta^{18}\text{O}$ ²³, **g** marine core 63KA $\Delta\delta^{18}\text{O}$ of *N. dutreii*—*G. sacculifer*⁶⁹, **h** Indian Sahiya stalagmite SAH-2 $\delta^{18}\text{O}$ ²⁸, **i** Gulf of Oman marine core M5-422 CaCO_3 ⁷¹, **j** Kotla Dahar lake $\delta^{18}\text{O}$ ¹⁹, and **k** Early Harappan (EH, c. 5.0–4.6 ka BP), Mature Harappan (MH, c. 4.6–3.9 ka BP), and Late Harappan (LH, c. 3.9–3.6 ka BP) periods, shown with interpreted favorability for summer and winter crop cultivation based on the climate records in the figure. Dates are shown above each record with $\pm 2\sigma$ error bars.

farming practices of some populations of the Indus Civilization made them more resilient to such changes^{10,11,75}.

Populations of the Indus Civilization were already adapted to cope with unpredictable climate conditions, and had the capacity to utilize a range of agricultural strategies involving both summer and winter crops^{10,75}. However, through an extended, multi-generational drought, such adaptation strategies would have become necessary measures of last-resort, leading to reduced surpluses, decreased margins of error, and elevated vulnerability to environmental hazards and rapid hydrological changes^{7,11,76}. Such changes are reflected in a reduction in craft activities and innovation in Indus urban centers, the decline of long-distance exchange and trade, and a trend towards deurbanization and the proliferation of smaller and more flexible rural settlements^{8,11}. The DHAR-1 record suggests that both summer and winter crops would have become increasingly challenging to grow after 4.2 ka BP, though an ISM recovery by 3.7 ka BP would have favored summer crops in ISM-dominated regions (Fig. 4k). Aridity-adapted crops like winter barley and summer millet would have been the most successful under these changed circumstances, while crop diversity (including rice, which continued being used in the Late Harappan and post-Indus period) would have helped mitigate risk. The likelihood that cropping strategies were designed to mitigate risk is supported by the available archaeological evidence^{7,8,11,75,77,78}. The observed decreasing reliance

on winter wheat after 4.2 ka BP and increasing presence of more drought-tolerant summer crops benefited smaller communities that were self-reliant^{11,79,80}, and perhaps even encouraged pastoralism^{8,81}. This socio-economic transformation was combined with a spatial displacement of population towards settlements in the ISM-dominated northeastern and southeastern Indus regions, which also offer a higher total annual rainfall¹⁰. In this respect, the stressors of a climatic shift with associated environmental changes over a multi-generational period would have led to sustainability through tactical and strategic subsistence choices, as well as adaptation through movement away from cities into new parts of the rural hinterland. The side effect of such strategic choices, however, was a transition away from an urban way of life that had seen the flourish of new technologies.

As the Late Harappan period transitioned into the Painted Grey Ware period after 3.5 ka BP, the DHAR-1 record suggests a state of increased seasonality between 3.97 and 3.4 ka BP, where summer crops may have been favored over winter crops (Fig. 4k), but there is little archaeological data available for this period as yet. From 3.4 to 3.1 ka BP, the trend may have reversed to a state of decreased seasonality with a weaker ISM and warmer/wetter winters. It was during this period that larger settlements began to appear at Charsadda, Taxila, and in the Bannu region, which all lie along the western edge of the Indus River Basin⁸². Larger settlements would develop in a range of locations in the Ganges

River Basin after 3.0 ka BP. The nature of adaptations in these later periods remain to be explored in detail, but together with the example of the Indus Civilization, they provide informative analogs for the modern situation where we again face a changing climate, albeit one that is largely being impacted by human actions.

Conclusions

The DHAR-1 paleoclimate record indicates that the 4.2 ka event consisted of three distinct dry phases that involved a decrease in both the Indian Summer Monsoon (ISM) and Indian Winter Monsoon (IWM). Prior studies have focused exclusively on either ISM or winter rainfall depending on their location, so additional multi-proxy studies from the overlapping region (particularly the western region, covering 5.0–3.0 ka BP) are critically needed to better understand the interaction of these two rainfall systems. The impact of the 4.2 ka event is especially detectable in north-west South Asia because the ISM and IWM domains overlap in this region, and both seasons were affected by decreased rainfall during the mid-late Holocene transition. The role of winter aridity is particularly noteworthy as it enhances and prolongs the driest growing season. The DHAR-1 record shows a 230-year period from 4.2 to 3.97 ka BP where all moisture proxies (ISM, PAP, and drip rate) unambiguously indicate aridity, punctuated by three 25–90 year-long phases of lower rainfall that lasted long enough to affect multiple generations of individual populations and their subsistence strategies. After 3.97 ka BP, diverging trends in these proxies suggest yearlong aridity was replaced by more complex shifts in rainfall seasonality and environmental conditions—including a recovery of the ISM by 3.7 ka BP alongside drier and/or cooler winters that may have also promoted a long-term ecological shift towards more drought-resistant grassy vegetation. Eventually, this may have increased waterlogging of soil above the cave to the point of altering local redox conditions. Shifting seasonality of precipitation appears to be a key factor influencing the populations in the Indus River Basin over the mid-late Holocene, encouraging cropping adaptations and shifting population centers based on the availability of food and water throughout the year.

Methods

Dating and mineralogy. U-series dating was performed at Caltech on 22 samples (Supplementary Table S2). No date has yet been analyzed from the calcite segment older than 4.14 ka BP due to a lack of specialized equipment needed for such small and very likely Th-rich samples. Twelve U-series ages (between 2.55 and 4.14 ka BP) were used to construct the final age model (Supplementary Fig. S4), which was built using ensembles of 2000 Monte Carlo simulations for each proxy using the MATLAB-based COPRA routine that explicitly considers individual proxy uncertainties⁵⁷. The Piecewise Cubic Hermite Interpolating Polynomial (PCHIP) interpolation method was used for all proxies. COPRA output has the distinct advantage of showing both the age uncertainties as well as confidence envelopes for all the proxy time series. X-ray diffraction (XRD) was used to check for mineralogical changes of aragonite v. calcite. Four 20 mg samples were milled from DHAR-1A, mixed with ethanol and evenly smeared onto a glass plate. Samples were loaded onto a Bruker D8 XRD instrument equipped with a MoK α source Lynxeye XE-T PSD detector. Measurements spanned 0–40° angle at 0.037° steps, 206.5 s per step. Phases were identified using the PDF2 (Powder Diffraction File) database in Eva V10.0 software.

Stable isotopes. Using the DHAR-1A half of the speleothem, 750 samples were milled for stable isotope analysis ($\delta^{18}\text{O}$ and $\delta^{13}\text{C}$) at 100–300 μm resolution and analyzed at GFZ Potsdam. Further high-resolution stable isotope analysis at the University of Cambridge included 876 samples from the bottom 4 cm of the mirroring slab DHAR-1B, covering c. 4.2–3.6 ka BP. In the high-resolution series, 74 samples were taken from the basal section of DHAR-1A because this portion of the speleothem is better represented and preserved on the DHAR-1A slab. As the mirror image of DHAR-1A, slab DHAR-1B is minimally offset (Supplementary Fig. S5). The curvature of the speleothem and the high-resolution nature of the stable isotope dataset from DHAR-1B (50 μm) renders some inevitable offsets, and requires adjustment prior to comparison of the high-resolution and lower-

resolution profiles. A master depth scale was created based on the LA-ICP-MS transects from slab DHAR-1B.

A Sherline micromill with a \varnothing 1 mm drill bit was used for stable isotope sub-sampling. Sampling lines were selected near the central drip point of the speleothem, where the laminations showed minimal curvature. To eliminate as much cross-sample integration error as possible during the high-resolution milling process, we first milled a 1 mm deep trench along the sampling lines, as well as a parallel trench 5 mm away from the sample line following established procedures²⁹ (Supplementary Fig. S5). All sampling equipment was cleaned with ethanol before each sample. An air duster was used to remove residual dust. This trenching process ultimately resulted in a 4-mm-wide section between the trenches that was sampled at 50 μm resolution, at 0.75 mm depth.

For each sample, c. 200 μg of material was milled, of which c. 100–200 μg were sealed in a Borosilicate glass exetainer vial with a silicone rubber septum, and loaded onto the Thermo Gasbench autosampler in batches of 40 samples. Each batch of samples included 10 reference carbonates of the in-house standard Carrara Z (calibrated to VPDB using the international standard NBS 19) and 2 control samples of Fletton Clay. Samples and standards were first flushed with helium and then acidified with 104% orthophosphoric acid for 1 h at 70 °C, and finally analyzed with a Thermo Delta V mass spectrometer in continuous flow mode. Precision of Carrara Z was $\pm 0.06\text{‰}$ (1σ) for $\delta^{18}\text{O}$ and $\delta^{13}\text{C}$.

To merge the isotope data from the aragonitic and calcitic parts of the stalagmite, a +1.16‰ carbon isotope correction and a +0.81‰ oxygen isotope correction⁸³ was applied to the measurements from the basal section of speleothem (247–250.3 mm) that consists primarily of calcite instead of aragonite. The original, uncorrected calcite data are reported in data files, but the corrected-to-aragonite data are plotted in all figures.

The $\delta^{44/40}\text{Ca}$ measurements were made on 60 samples of aragonite and 1 sample of calcite milled along the stalagmite growth axis between 4.2–2.8 ka BP. Of these samples, 23 were initially milled at point locations on the DHAR-1A slab, followed up by 38 high-resolution measurements on the DHAR-1B slab focused on the period 4.2–3.6 ka BP (achieving a resolution of one sample per 12.6 years in this period). In addition, cave host rock (–0.36‰), drip water (–0.43‰), and modern carbonate samples (mean of –0.78‰) were measured. The $\delta^{44/40}\text{Ca}$ measurements were made on a ThermoFisher Scientific Triton Plus Multicollector Thermal Ionization Mass Spectrometer (MC-TIMS) at the University of Cambridge following established methods⁸⁴. Carbonate samples were dissolved in 2% nitric acid, and a double spike of ^{42}Ca and ^{48}Ca (1:1) was added to a 10:1 sample to spike ratio. A dose of c. 4 μg of Ca was loaded onto double rhenium filaments and activated with phosphoric acid. The NIST 915 A or 915B standard was measured about every 10 samples, and yielded a 2σ error of 0.1‰ for 11 total measurements.

Trace element analysis. The elemental composition of DHAR-1B was determined using laser ablation inductively-coupled plasma mass spectrometry (LA-ICP-MS). Elemental data was measured at the University of Waikato under supervision of Dr. Amanda French. The speleothem was ablated using a RESOLUTION SE series 193 nm excimer laser ablation system. Helium was used as the carrier gas to move the aerosol to an Agilent 8900 Triple-Quad ICP-MS. DHAR-1B was ablated using a 50 μm diameter laser spot size, which traversed the speleothem parallel to the growth axis at 24.3 $\mu\text{m}/\text{second}$ to achieve a final spatial resolution of c. 25 μm . Before the measurement, each line was traversed by a rapid 100 μm spot size laser ablation cleaning sweep to remove potential contaminants. For the base of slab DHAR-1B, sampling was done parallel to the sampling tracks generated for the stable isotope milling, and beyond this the laser ablation analysis was continued along the growth axis in 8 segments (Supplementary Fig. S5). The glass standards NIST610 and NIST612 bracketed measurement transects at least every 15 min to correct for instrumental drift. Raw data was processed using the IOLITE data-processing software⁸⁵, and trace element/Ca mass ratios were calculated using Ca as an internal standard assuming stoichiometry (40% Ca in CaCO_3).

The LA-ICP-MS data was further post-processed in MATLAB to remove any obvious outliers by identifying points $\pm 4\sigma$ away from a 5-point running mean of the dataset. The software program PAST 4.10 (Hammer et al., 2001) was used for the principal component analysis (Fig. 3). We used 16 of the element ratios over the time interval 4.2–3.1 ka BP in the aragonite portion of the speleothem (Ba/Ca, Co/Ca, Cr/Ca, Cu/Ca, Fe/Ca, K/Ca, Mg/Ca, Mn/Ca, Ni/Ca, Pb/Ca, S/Ca, Si/Ca, Sr/Ca, Ti/Ca, U/Ca, and Zn/Ca). The correlation matrix was used to compare standardized variables, and a Kaiser–Meyer–Olkin value of 0.84 indicates that the dataset and sampling resolution is well-suited for principal component analysis. PC1 explains 28.8% of the variance, highlighting the unique properties of U/Ca compared to the rest of the elements (a strong effect of PAP). PC2 explains 12.4% of the total variance (highlighting the PAP v. transition metal element clusters), and PC3 explains 9% of the variance (distinguishing the detrital/weathering/redox indicators).

Data availability

The datafiles for producing the charts and graphs of this manuscript are deposited in the Apollo repository at the University of Cambridge (<https://doi.org/10.17863/CAM.95036>). The data are also available in the PANGAEA repository (<https://doi.pangaea.de/10.1594/PANGAEA.956928>).

Received: 21 December 2021; Accepted: 17 March 2023;

Published online: 04 April 2023

References

- Riedel, N. et al. Monsoon forced evolution of savanna and the spread of agropastoralism in peninsular India. *Sci. Rep.* **11**, 1–13 (2021).
- Kwiecien, O. et al. What we talk about when we talk about seasonality—a transdisciplinary review. *Earth Sci. Rev.* **225**, 103843 (2022).
- Overpeck, J., Anderson, D., Trumbore, S. & Prell, W. The southwest Indian Monsoon over the last 18000 years. *Clim. Dyn.* **12**, 213–225 (1996).
- Fleitmann, D. et al. Holocene forcing of the Indian monsoon recorded in a stalagmite from southern Oman. *Science* **300**, 1737–1739 (2003).
- Herzschuh, U. Palaeo-moisture evolution in monsoonal Central Asia during the last 50,000 years. *Quat. Sci. Rev.* **25**, 163–178 (2006).
- Wang, Y., Liu, X. & Herzschuh, U. Asynchronous evolution of the Indian and East Asian Summer Monsoon indicated by Holocene moisture patterns in monsoonal central Asia. *Earth Sci. Rev.* **103**, 135–153 (2010).
- Madella, M. & Fuller, D. Q. Palaeoecology and the Harappan Civilisation of South Asia: a reconsideration. *Quat. Sci. Rev.* **25**, 1283–1301 (2006).
- Wright, R. P. *The ancient Indus: Urbanism, economy, and society* (Cambridge: Cambridge University Press, 2010).
- Schug, G. R., Blevins, K. E., Cox, B., Gray, K. & Mushrif-Tripathy, V. Infection, disease, and biosocial processes at the end of the Indus Civilization. *PLoS One* **8**, e8481 (2013).
- Petrie, C. A. et al. Adaptation to variable environments, resilience to climate change: Investigating land, water and settlement in Indus Northwest India. *Curr. Anthropol.* **58**, 1–30 (2017).
- Petrie, C. A. Diversity, variability, adaptation and ‘fragility’ in the Indus Civilization. In *The evolution of fragility: setting the terms* (ed. Yoffee, N.) 109–134 (McDonald Institute for Archaeological Research, 2019).
- Chase, B., Meiggs, D. & Ajithprasad, P. Pastoralism, climate change, and the transformation of the Indus Civilization in Gujarat: Faunal analyses and biogenic isotopes. *J. Anthropol. Archaeol.* **59**, 101173 (2020).
- Dimri, A. P., Yasunari, T., Kotlia, B. S., Mohanty, U. C. & Sikka, D. R. Indian winter monsoon: present and past. *Earth Sci. Rev.* **163**, 297–322 (2016).
- Ronay, E. R., Breitenbach, S. F. & Oster, J. L. Sensitivity of speleothem records in the Indian Summer Monsoon region to dry season infiltration. *Sci. Rep.* **9**, 1–10 (2019).
- Bolch, T. et al. The state and fate of Himalayan glaciers. *Science* **336**, 310–314 (2012).
- Immerzeel, W. W., Droogers, P., De Jong, S. M. & Bierkens, M. F. P. Large-scale monitoring of snow cover and runoff simulation in Himalayan river basins using remote sensing. *Remote Sens. Environ.* **113**, 40–49 (2009).
- Singh, G., Joshi, R. D., Chopra, S. K. & Singh, A. B. Late Quaternary history of vegetation and climate of the Rajasthan Desert, India. *Philos. Trans. R. Soc. Lond. B, Biol. Sci.* **267**, 467–501 (1974).
- Staubwasser, M., Sirocko, F., Grootes, P. M. & Segl, M. Climate change at the 4.2 ka BP termination of the Indus valley civilization and Holocene south Asian monsoon variability. *Geophys. Res. Lett.* **30**, 1–4 (2003).
- Dixit, Y., Hodell, D. A. & Petrie, C. A. Abrupt weakening of the summer monsoon in northwest India~ 4100 yr ago. *Geology* **42**, 339–342 (2014).
- Dixit, Y. et al. Intensified summer monsoon and the urbanization of Indus Civilization in northwest India. *Sci. Rep.* **8**, 1–8 (2018).
- Bar-Matthews, M. & Ayalon, A. Mid-Holocene climate variations revealed by high-resolution speleothem records from Soreq Cave, Israel and their correlation with cultural changes. *Holocene* **21**, 163–171 (2011).
- Wick, L., Lemcke, G. & Sturm, M. Evidence of Lateglacial and Holocene climatic change and human impact in eastern Anatolia: high-resolution pollen, charcoal, isotopic and geochemical records from the laminated sediments of Lake Van, Turkey. *Holocene* **13**, 665–675 (2003).
- Carolin, S. A. et al. Precise timing of abrupt increase in dust activity in the Middle East coincident with 4.2 ka social change. *Proc. Natl. Acad. Sci. USA* **116**, 67–72 (2019).
- Dykoski, C. A. et al. A high-resolution, absolute-dated Holocene and deglacial Asian monsoon record from Dongge Cave, China. *Earth Planet. Sci. Lett.* **233**, 71–86 (2005).
- Berkelhammer, M. et al. An abrupt shift in the Indian monsoon 4000 years ago. *Geophys. Monogr. Ser.* **198**, 75–87 (2012).
- Yang, X. et al. Groundwater sapping as the cause of irreversible desertification of Hunshandake Sandy Lands, Inner Mongolia, northern China. *Proc. Natl. Acad. Sci. USA* **112**, 702–706 (2015).
- Kathayat, G. et al. Evaluating the timing and structure of the 4.2 ka event in the Indian summer monsoon domain from an annually resolved speleothem record from Northeast India. *Clim. Past* **14**, 1869–1879 (2018).
- Kathayat, G. et al. The Indian monsoon variability and civilization changes in the Indian subcontinent. *Sci. Adv.* **3**, e1701296 (2017).
- Lechleitner, F. A. et al. Climatic and in-cave influences on $\delta^{18}\text{O}$ and $\delta^{13}\text{C}$ in a stalagmite from northeastern India through the last deglaciation. *Quat. Res.* **88**, 458–471 (2017).
- Fohlmeister, J. Main controls on the stable carbon isotope composition of speleothems. *Geochim. Cosmochim. Acta* **279**, 67–87 (2020).
- Delaygue, G. et al. Oxygen isotope/salinity relationship in the northern Indian Ocean. *J. Geophys. Res. Oceans* **106**, 4565–4574 (2001).
- Sengupta, S. & Sarkar, A. Stable isotope evidence of dual (Arabian Sea and Bay of Bengal) vapour sources in monsoonal precipitation over north India. *Earth Planet. Sci. Lett.* **250**, 511–521 (2006).
- Bhattacharya, S. K., Froehlich, K., Aggarwal, P. K., Kulkarni, K. M. Isotopic variation in Indian Monsoon precipitation: records from Bombay and New Delhi. *Geophys. Res. Lett.* **30**, 1–4 (2003).
- Dansgaard, W. Stable isotopes in precipitation. *Tellus* **16**, 436–468 (1964).
- Breitenbach, S. F. et al. Strong influence of water vapor source dynamics on stable isotopes in precipitation observed in Southern Meghalaya, NE India. *Earth Planet. Sci. Lett.* **292**, 212–220 (2010).
- Hunt, K. M., Turner, A. G. & Shaffrey, L. C. Extreme daily rainfall in Pakistan and north India: Scale interactions, mechanisms, and precursors. *Mon. Weather Rev.* **146**, 1005–1022 (2018).
- Baudouin, J. P., Herzog, M. & Petrie, C. A. Synoptic processes of winter precipitation in the Upper Indus Basin. *Weather Clim. Dyn.* **2**, 1187–1207 (2021).
- Dimri, A. P. The transport of momentum, sensible heat, potential energy and moisture over the western Himalayas during the winter season. *Theor. Appl. Climatol.* **90**, 49–63 (2007).
- Dimri, A. P. & Chevuturi, A. *Western disturbances—an Indian meteorological perspective* (Springer International Publishing, 2016).
- Sanwal, J. et al. Climatic variability in Central Indian Himalaya during the last~ 1800 years: evidence from a high resolution speleothem record. *Quat. Int.* **304**, 183–192 (2013).
- Khan, I., Amir, M., Paul, D. & Srivastava, P. Late Holocene aridification recorded in the stable carbon and nitrogen isotope composition of soils from Nainital, Lesser Himalaya. *Quat. Int.* **467**, 195–203 (2018).
- Khan, I. et al. Late Pleistocene–Holocene vegetation and climate variability of the western Himalaya, India. *J. Asian Earth Sci.* **233**, 105245 (2022).
- Sigdel, S. R., Dawadi, B., Camarero, J. J., Liang, E. & Leavitt, S. W. Moisture-limited tree growth for a subtropical Himalayan conifer forest in Western Nepal. *Forests* **9**, 340 (2018).
- Tiwari, A., Thapa, N., Aryal, S., Rana, P. & Adhikari, S. Growth performance of planted population of *Pinus roxburghii* in central Nepal. *J. Ecol. Environ.* **44**, 1–11 (2020).
- Yadav, R. R., Misra, K. G., Kotlia, B. S. & Upreti, N. Premonsoon precipitation variability in Kumaon Himalaya, India over a perspective of~ 300 years. *Quat. Int.* **325**, 213–219 (2014).
- Rai, S. et al. Growth response of *Abies spectabilis* to climate along an elevation gradient of the Manang valley in the central Himalayas. *J. For. Res.* **31**, 2245–2254 (2020).
- Owen, R. A. et al. Calcium isotopes in caves as a proxy for aridity: Modern calibration and application to the 8.2 kyr event. *Earth Planet. Sci. Lett.* **443**, 129–138 (2016).
- Magiera, M. et al. Local and regional Indian Summer Monsoon precipitation dynamics during Termination II and the Last Interglacial. *Geophys. Res. Lett.* **46**, 12454–12463 (2019).
- de Wet, C. B. et al. Semiquantitative estimates of rainfall variability during the 8.2 kyr event in California using speleothem calcium isotope ratios. *Geophys. Res. Lett.* **48**, e2020GL089154 (2021).
- Fairchild, I. J. & Treble, P. C. Trace elements in speleothems as recorders of environmental change. *Quat. Sci. Rev.* **28**, 449–468 (2009).
- Fairchild, I. J. et al. Controls on trace element (Sr–Mg) compositions of carbonate cave waters: implications for speleothem climatic records. *Chem. Geol.* **166**, 255–269 (2000).
- Johnson, K. R., Hu, C., Belshaw, N. S. & Henderson, G. M. Seasonal trace-element and stable-isotope variations in a Chinese speleothem: The potential for high-resolution paleomonsoon reconstruction. *Earth Planet. Sci. Lett.* **244**, 394–407 (2006).
- Jamieson, R. A. et al. Intra- and inter-annual uranium concentration variability in a Belizean stalagmite controlled by prior aragonite precipitation: a new tool for reconstructing hydro-climate using aragonitic speleothems. *Geochim. Cosmochim. Acta* **190**, 332–346 (2016).
- Wassenburg, J. A. et al. Determination of aragonite trace element distribution coefficients from speleothem calcite–aragonite transitions. *Geochim. Cosmochim. Acta* **190**, 347–367 (2016).
- Hartland, A. & Zitoun, R. Transition metal availability to speleothems controlled by organic binding ligands. *Geochem. Perspect. Lett.* **8**, 22–25 (2018).

56. Lindeman, I., Hansen, M., Scholz, D., Breitenbach, S. F. M. & Hartland, A. Effects of organic matter complexation on partitioning of transition metals into calcite: cave-analogue crystal growth experiments. *Geochim. Cosmochim. Acta* **317**, 118–137 (2022).
57. Breitenbach, S. F. et al. Constructing proxy records from age models (COPRA). *Clim. Past* **8**, 1765–1779 (2012).
58. Frisia, S., Borsato, A., Fairchild, I. J., McDermott, F. & Selmo, E. M. Aragonite-calcite relationships in speleothems (Grotte de Clamouse, France): environment, fabrics, and carbonate geochemistry. *J. Sediment. Res.* **72**, 687–699 (2002).
59. Railsback, L. B. et al. Petrographic and isotopic evidence for Holocene long-term climate change and shorter-term environmental shifts from a stalagmite from the Serra do Courel of northwestern Spain, and implications for climatic history across Europe and the Mediterranean. *Palaeogeogr. Palaeoclimatol. Palaeoecol.* **305**, 172–184 (2011).
60. Wassenburg, J. A. et al. Climate and cave control on Pleistocene/Holocene calcite-to-aragonite transitions in speleothems from Morocco: Elemental and isotopic evidence. *Geochim. Cosmochim. Acta* **92**, 23–47 (2012).
61. Kotlia, B. S., Singh, A. K., Joshi, L. M. & Bisht, K. Precipitation variability over Northwest Himalaya from ~4.0 to 1.9 ka BP with likely impact on civilization in the foreland areas. *J. Asian Earth Sci.* **162**, 148–159 (2018).
62. Stumm, W., Morgan, J. J. *Aquatic chemistry: chemical equilibria and rates in natural waters*, vol. 126, (John Wiley & Sons, 2012).
63. Singh, A., Thakur, S. & Adhikary, N. C. Influence of climatic indices (AMO, PDO, and ENSO) and temperature on rainfall in the Northeast Region of India. *SN Appl. Sci.* **2**, 1–15 (2020).
64. Bini, M. et al. The 4.2 ka BP Event in the Mediterranean region: an overview. *Clim. Past* **15**, 555–577 (2019).
65. Perçou, A., Ionita, M. & Weiss, H. Atmospheric blocking induced by the strengthened Siberian High led to drying in west Asia during the 4.2 ka BP event—a hypothesis. *Clim. Past* **15**, 781–793 (2019).
66. Myers, C. G. et al. Northeast Indian stalagmite records Pacific decadal climate change: implications for moisture transport and drought in India. *Geophys. Res. Lett.* **42**, 4124–4132 (2015).
67. Malik, A. et al. Decadal to multi-decadal scale variability of Indian summer monsoon rainfall in the coupled ocean-atmosphere-chemistry climate model SOCOL-MPIOM. *Clim. Dyn.* **49**, 3551–3572 (2017).
68. Basu, S. et al. Variation in monsoonal rainfall sources (Arabian Sea and Bay of Bengal) during the late Quaternary: Implications for regional vegetation and fluvial systems. *Palaeogeogr. Palaeoclimatol. Palaeoecol.* **491**, 77–91 (2018).
69. Giesche, A., Staubwasser, M., Petrie, C. A. & Hodell, D. A. Indian winter and summer monsoon strength over the 4.2 ka BP event in foraminifer isotope records from the Indus River delta in the Arabian Sea. *Clim. Past* **15**, 73–90 (2019).
70. Arz, H. W., Lamy, F. & Pätzold, J. A pronounced dry event recorded around 4.2 ka in brine sediments from the northern Red Sea. *Quat. Res.* **66**, 432–441 (2006).
71. Cullen, H. M. et al. Climate change and the collapse of the Akkadian empire: evidence from the deep sea. *Geology* **28**, 379–382 (2000).
72. Demske, D., Tarasov, P. E., Wünnemann, B. & Riedel, F. Late glacial and Holocene vegetation, Indian monsoon and westerly circulation in the Trans-Himalaya recorded in the lacustrine pollen sequence from Tso Kar, Ladakh, NW India. *Palaeogeogr. Palaeoclimatol. Palaeoecol.* **279**, 172–185 (2009).
73. Menzel, P. et al. Linking Holocene drying trends from Lonar Lake in monsoonal central India to North Atlantic cooling events. *Palaeogeogr. Palaeoclimatol. Palaeoecol.* **410**, 164–178 (2014).
74. Prasad, S. et al. Holocene climate forcings and lacustrine regime shifts in the Indian summer monsoon realm. *Earth Surf. Process. Landf.* **45**, 3842–3853 (2020).
75. Petrie, C. A. & Bates, J. ‘Multi-cropping’, intercropping and adaptation to variable environments in Indus South Asia. *J. World Prehist.* **30**, 81–130 (2017).
76. Giosan, L. et al. Fluvial landscapes of the Harappan civilization. *Proc. Natl. Acad. Sci. USA* **109**, E1688–E1694 (2012).
77. Weber, S. A. Archaeobotany at Harappa: indications for change. In *Indus Ethnobiology: new perspectives from the field*, (eds. Weber, S. A. & Belcher, W. R.) 175–198 (Lexington, 2003).
78. Pokharia, A. K. et al. Altered cropping pattern and cultural continuation with declined prosperity following abrupt and extreme arid event at ~4,200 yrs BP: Evidence from an Indus archaeological site Khirsara, Gujarat, western India. *PLoS One* **12**, e0185684 (2017).
79. Weber, S. A., Kashyap, A. & Harriman, D. Does size matter: the role and significance of cereal grains in the Indus civilization. *Archaeol. Anthropol. Sci.* **2**, 35–43 (2010).
80. Sarkar, A. et al. Oxygen isotope in archaeological bioapatites from India: implications to climate change and decline of Bronze Age Harappan civilization. *Sci. Rep.* **6**, 1–9 (2016).
81. Miller, L. J. *Urban economies in early states: the Secondary Products Revolution in the Indus civilization* (New York University, 2004).
82. Petrie, C. A. *Resistance at the edge of empires: the archaeology and history of the Bannu Basin from 1000 BC to AD 1200* (Oxbow Books, 2020).
83. Fohlmeister, J. et al. Carbon and oxygen isotope fractionation in the water-calcite-aragonite system. *Geochim. Cosmochim. Acta* **235**, 127–139 (2018).
84. Bradbury, H. J. & Turchyn, A. V. Calcium isotope fractionation in sedimentary pore fluids from ODP Leg 175: Resolving carbonate recrystallization. *Geochim. Cosmochim. Acta* **236**, 121–139 (2018).
85. Paton, C., Hellstrom, J., Paul, B., Woodhead, J. & Hergt, J. Iolite: freeware for the visualisation and processing of mass spectrometric data. *J. Anal. At. Spectrom.* **26**, 2508–2518 (2011).
86. Meyer-Christoffer, A., Becker, A., Finger, P., Schneider, U. & Ziese, M. Data from “GPCC climatology version 2018 at 0.25°: monthly land-surface precipitation climatology for every month and the total year from rain-gauges built on GTS-based and historical data.” GPCC at DWD. https://doi.org/10.5676/DWD_GPCC/CLIM_M_V2018_025, Deposited (2018).
87. Hammer, Ø., Harper, D. A. T. & Ryan, P. D. PAST: Paleontological Statistics software package for education and data analysis. *Palaeontol. Electron.* **4**, 1–9 (2001).

Acknowledgements

The authors would like to thank Dr. Giulio Lampronti for assistance with XRD measurements at the University of Cambridge. N.M. received financial support from the German Science Foundation (DFG projects MA4759/9-1 and MA4759/11-1). A.G., D.A.H., and C.A.P. received support from the European Research Council (ERC) under the European Union's Horizon 2020 research and innovation program (grant agreement no 648609). A.G., A.H. and S.F.M.B. received support from the European Union's Horizon 2020 program (QUEST project, grant agreement no 691037), C.A.P. received funding from the Global Challenges Research Fund's TIGR2ESS project (BB/P027970/1), and A.H. was further supported by Rutherford Discovery Fellowship (RDF-UOW1601) awarded by Royal Society Te Aparangi. Calcium isotope analyses were supported through NERC NE/R013519/1 (H.J.B.). No permissions were required for sampling, but we gratefully acknowledge the support of the local village leaders and accompanying guide.

Author contributions

A.G., D.A.H., C.A.P., and S.F.M.B. designed research; A.G., S.F.M.B., A.D.F., H.J.B., G.H.H., J.F.A., B.P., and N.M. performed research; A.G., A.H., D.A.H., and S.F.M.B. analyzed data; A.G. and S.F.M.B. prepared figures; A.G., D.A.H., C.A.P., H.J.B., and S.F.M.B. wrote the paper.

Competing interests

The authors declare no competing interests.

Additional information


Supplementary information The online version contains supplementary material available at <https://doi.org/10.1038/s43247-023-00763-z>.

Correspondence and requests for materials should be addressed to Alena Giesche.

Peer review information *Communications Earth & Environment* thanks Yiming Wang and the other, anonymous, reviewer(s) for their contribution to the peer review of this work. Primary Handling Editors: Michael Storozum and Joe Aslin.

Reprints and permission information is available at <http://www.nature.com/reprints>

Publisher's note Springer Nature remains neutral with regard to jurisdictional claims in published maps and institutional affiliations.

 **Open Access** This article is licensed under a Creative Commons Attribution 4.0 International License, which permits use, sharing, adaptation, distribution and reproduction in any medium or format, as long as you give appropriate credit to the original author(s) and the source, provide a link to the Creative Commons license, and indicate if changes were made. The images or other third party material in this article are included in the article's Creative Commons license, unless indicated otherwise in a credit line to the material. If material is not included in the article's Creative Commons license and your intended use is not permitted by statutory regulation or exceeds the permitted use, you will need to obtain permission directly from the copyright holder. To view a copy of this license, visit <http://creativecommons.org/licenses/by/4.0/>.

© The Author(s) 2023